Applied Acoustics 240 (2025) 110928

Contents lists available at ScienceDirect

Applied Acoustics

journal homepage: www.elsevier.com/locate/apacoust

Quasi-compact model for accurate noise prediction of complex rotor configurations

F. Caccia [a,*], L. Galimberti [a,b], L. Abergo [a], A. Savino [a], A. Zanotti [a], M. Parsani [b,c], A. Guardone [a]

[a] Politecnico di Milano, Dipartimento di Scienze e Tecnologie Aerospaziali, via La Masa 34, 20156, Milan, Italy
[b] Computer Electrical and Mathematical Science and Engineering Division (CEMSE), King Abdullah University of Science and Technology, Thuwal, Saudi Arabia
[c] Physical Science and Engineering Division (PSE), King Abdullah University of Science and Technology, Thuwal, Saudi Arabia

ARTICLE INFO

Keywords:
Aeroacoustics
Propeller noise
Rotor-wake interaction
Blade-vortex interaction
Vortex particle method
Acoustic compactness

ABSTRACT

The design of urban air mobility systems requires fast yet accurate aerodynamic and acoustic analyses of propeller interactions. Low-fidelity solvers relying on compact F1A formulations are commonly used, but the compact acoustic assumption does not hold for loading noise produced by unsteady inflows. This study introduces a quasi-compact acoustic model applied to isolated and tandem interacting propellers comparing its performance against other hybrid solvers. The quasi-compact model propagates the local chord-wise and span-wise pressure jump distribution computed with a non-linear vortex-lattice aerodynamic solution to far-field observers. Compact models simplify this by using the span-wise distribution only. Reference solutions are generated by propagating high-fidelity CFD pressure fields to far-field observers using the same Ffowcs Williams-Hawkings solver. Results demonstrate that the compact formulation achieves convergence only for isolated propellers, whereas the quasi-compact formulation can provide converged solutions also with rotor-rotor interactions and compares better with the reference high-fidelity data.

1. Introduction

In the urban air mobility (UAM) market, industrial partners and research institutes are developing unconventional designs for electric vertical take-off and landing (eVTOL) aircraft. Distributed electric propulsion is established as common grounds of development and, as such, multirotor architectures [1,2], and layouts combining multiple wings are a reality. Despite the numerous designs, most solutions embrace complex configurations with more than one lifting surface and multiple engines. As a result, many multidisciplinary challenges are affecting the design process.

The compliance of many interaction effects represents the biggest hurdle for aerodynamic design. Multirotor interaction, wake-body interaction, interaction between fixed wings, etc., collectively concur to increase the modeling and optimization task. Although such physical phenomena are segregated for conventional aircraft architectures, for eVTOL applications, they strongly alter aircraft performances, handling qualities, and certainly noise generation. Noise assessment is essential to the certification process since eVTOL missions are mainly located in urban areas. Recent literature reports just a few works concerning rotor-rotor aerodynamic interaction with application to UAV or small drones, e.g., [3] and [4]. While the industry is challenged to build commercially viable aircraft, academia is endowed with the quest to fill the knowledge gap concerning the complex aerodynamic and aeroacoustics of multi-rotor systems, providing fast and accurate tools for designing high-performance aircraft that fulfill strict noise impact requirements.

One of the major sources of noise pollution from eVTOLs is the rotational tonal noise emitted by propellers. This noise results from two source terms, i.e., a monopole term named thickness noise due to the displacement of fluid produced by the body, and a dipole term called loading noise due to the steady and unsteady loading exerted by the body on the fluid as seen from a fixed observer. Loading noise becomes predominant with highly loaded blades or strong impulsive phenomena such as blade-vortex interaction (BVI). Due to the low-subsonic operating tip-Mach number, the quadrupole term related to the non-linear volume sources is generally disregarded. Another relevant noise source is broadband noise related to surface loading and generated by higher-frequency, non-deterministic pressure fluctuations. Still, its study is outside the scope of this work.

* Corresponding author.
E-mail address: francescoangelo.caccia@polimi.it (F. Caccia).

https://doi.org/10.1016/j.apacoust.2025.110928
Received 18 February 2025; Received in revised form 2 June 2025; Accepted 3 July 2025
Available online 10 July 2025

Nomenclature

A	local element area	m^2
$\mathbf{A}$	matrix of influence coefficients	m^{-1}
$\boldsymbol{b}$	vector of boundary conditions enforced in NL-VL method	$m\,s^{-1}$
C_P	power coefficient, $C_P = P/(\rho_\infty n^3 D^5)$	
C_T	thrust coefficient, $C_T = T/(\rho_\infty n^2 D^4)$	
$C_{L/\alpha}$	lift curve slope in the linear range	
c	speed of sound	$m\,s^{-1}$
$\tilde{c}$	chord of VL strip	m
D	propeller diameter	m
$\boldsymbol{F}$	aerodynamic force	N
J	advance ratio, $J = U_\infty/(nD)$	
L	sectional lift	N
L_x	stream-wise distance between the propeller disks	m
L_y	lateral distance between the propeller axis	m
M	Mach number vector	
n	rotational speed	$rev\,s^{-1}$
$\hat{\boldsymbol{n}}$	unit normal vector	
P	propeller power	W
P_{ij}	fluid compressive stress tensor component	Pa
p	pressure	Pa
p'	acoustic pressure, $p' = p - p_0$	Pa
p_{ref}	reference pressure for SPL, $p_{\text{ref}} = 20\,\mu\text{Pa}$	
R	propeller radius	m
r	source-observer distance; $r_i = r\hat{r}_i$	m
$\hat{\boldsymbol{r}}$	unit source-observer vector	
S_b	body surface	
S_m	blade mid-plane surface	
SPL	sound pressure level	dB
t	observer time	s
$\hat{\boldsymbol{t}}$	unit chord-wise vector	
T	propeller thrust	N
$\mathcal{T}$	air temperature	K
$\boldsymbol{U}$	air velocity	$m\,s^{-1}$
$\boldsymbol{u}$	total velocity, including free-stream, body, and induced velocity	$m\,s^{-1}$
$\boldsymbol{u}_{2D}$	velocity projected on section plane	$m\,s^{-1}$
$\boldsymbol{u}_{tot\setminus v_{nl}}$	velocity induced by non-VL elements	$m\,s^{-1}$
$u_{v_{nl}}$	velocity induced by VL elements	$m\,s^{-1}$
$\boldsymbol{u}_\phi$	potential velocity	$m\,s^{-1}$
$\boldsymbol{u}_\psi$	perturbation velocity	$m\,s^{-1}$
$\boldsymbol{v}$	body velocity	$m\,s^{-1}$
xy	first observer lateral plane	
xz	second observer lateral plane	
yz	rotor-disk observer plane	
α	sectional blade angle of attack	°
β	blade pitch angle at 75% of the rotor radius	°
$\boldsymbol{\Gamma}$	vector of panel circulations	$m^2\,s^{-1}$
δ_{ij}	Kronecker delta	
ΔP	pressure jump across a vortex-lattice element; $\Delta P_i = \Delta P \hat{n}_i$	Pa
$\boldsymbol{\Delta D}^{\text{v}}$	viscous drag correction	N
θ_{ij}	observer position in plane ij	°
ρ	air density	$kg\,m^{-3}$
τ	retarded time, $\tau = t - r/c_0$	s
ψ	blade azimuthal angle	°
ω	vorticity magnitude	s^{-1}
Ω	rotational speed	RPM

Indices

$()_s$	suction-side variables
$()_p$	pressure-side variables
$()^i$	i^{th} non-linear vortex-lattice iteration
$()_k$	k^{th} vortex-lattice panel
$()_{\text{sec}}$	NL-VL strip (i.e. section) variable
$()_i$	i^{th} vector component
$()_\infty$	freestream value
$()_0$	reference value in undisturbed medium
$()'$	variable perturbation, $()' = () - ()_0$
$()_{\text{Lj}}$	loading noise component, $j = 1, 2, 3$
$()_{\text{Tj}}$	thickness noise component, $j = 1, 2$
$()_{\text{ret}}$	evaluated at retarded time τ

The search for reduced-order models for computing propeller noise has been going on for a long time [5]. Nowadays, compact models are required to analyze increasingly complex problems. For instance, Yunus et al. [6] developed an efficient low-fidelity model by using a blade element momentum aerodynamic model for tonal noise source characterization propagated via a compact source formulation by Casalino et al. [7] while also modeling the broadband trailing edge noise. The model was used for the parametric design of a rotor blade and in more recent work to assess the acoustic footprint of an eVTOL mission in an urban environment [8]. On the other hand, studying complex configurations with rotor-rotor interactions may require more accurate tools, retaining the efficiency of compact formulations to analyze large design spaces.

Specifically, the thickness noise generated by a blade section can be approximated using a source-sink pair with a strength corresponding to the one generated by the maximum thickness of the section, with a second-order effect given by the thickness distribution [5]. On the other hand, the loading noise can be computed from a sectional load "by introducing any chord-wise pressure distribution complying with the given sectional lift" under two assumptions, i.e., "chord length negligible with respect to the source–observer distance" and "limited values of chord-wise pressure gradients" [9]. A clear example is provided by the compact model by Casalino et al. [7] used in the aforementioned works. Moreover, as highlighted once more by Bernardini et al. [9], results obtained with compact models inherently lack accuracy in the rotor disk plane when chord-wise pressure gradients are not limited. To overcome these limitations, they proposed to reconstruct the chord-wise distribution of the pressure jump as a superposition of shape functions using the Küssner–Schwarz general theory for thin airfoil aerodynamics, requiring the knowledge of sectional lift, pitching moment, and higher-order moments for each section, or the downwash distribution along the blade surface. Nevertheless, the use of incompressible two-dimensional shape functions could provide a less accurate evaluation of the blade airfoils interactions with high frequency gusts.

More recently [10], a vortex lattice model has been coupled with a compact form of Farassat's formulation 1A using the monopole approximation proposed by Lopes [11], showing that the numerical method can accurately match aerodynamic loads and noise emission of a small isolated propeller measured in the NASA Langley's Low-Speed Acoustic Wind Tunnel facility. A similar effort by Jo et al. [12] applied a non-linear vortex lattice method to an isolated propeller for aerodynamic and tonal acoustic prediction. After analyzing the influence of space and time discretization on noise emission, emphasis was put on using time-averaged or instantaneous pressure distributions and the effect on the emitted spectrum. The acoustic propagation was made directly from the vortex-lattice panels, using what we name "quasi-compact" model. Indeed, each blade section is no longer condensed into a single point, but is represented as a set of points lying on the section mean line. We highlight that these works analyzed isolated propellers with a steady inflow.

A quasi-compact model, i.e., the noise propagation from an unsteady non-linear vortex-lattice aerodynamic solution, has clear specific advantages when compared to classic lifting-line and compact models, but they have not been previously addressed in the literature and will be considered in this work. First, the model can directly capture chord-wise pressure gradients, which are relevant, for instance, with unsteady inflows and during blade-vortex interaction. Second, the model can carry information about the thickness distribution of the blade sections recovering second-order thickness noise effects. Third, the convergence of the perceived acoustic signal can be guaranteed using an appropriate spatial discretization of the noise source. Compared to the work by Bernardini et al. [9] where analogous issues about compact models were addressed, here we directly compute the pressure jump distribution within the aerodynamic solver, and do not reconstruct a chord-wise global approximation of the pressure jump a-posteriori.

To show this, in this work, the propeller noise emission is predicted by comparing the compact and quasi-compact formulations with high-fidelity CFD data, showing their effectiveness and limitations for isolated and tandem configurations. In particular, this work considers a challenging, realistic condition with notable aerodynamic complexity, including highly pitched blades for forward flight with flow separation, tandem rotors, and highly nonuniform inflows. The test case reproduces the experimental activity described in [13], where scaled tandem propeller models with different degrees of overlap between rotor disks were investigated through wind tunnel measurements performed for typical cruise conditions of a tilting eVTOL concept. Preliminary aerodynamic and aeroacoustics results on these test cases were presented in [14] using simpler numerical models. The reference aerodynamic solution is obtained by solving the unsteady Reynolds-Averaged Navier-Stokes (uRANS) equations. Then, the same aeroacoustic code is used to propagate the reference aerodynamic solutions and the solutions obtained with a lifting line (compact) and a non-linear vortex-lattice (quasi-compact) method to far-field observers. The code solves a particular form of the Ffowcs-Williams Hawkings (FWH) equation generalized to moving surfaces [15]. The aeroacoustic code has been previously verified against analytical solutions and validated by comparing high-fidelity simulations against experiments [16,17].

The remainder of this paper is structured as follows. In Sec. 2, the methodology is presented with details on the non-linear vortex-lattice aerodynamic model (Sec. 2.1) and on the quasi-compact aeroacoustic formulation (Sec. 2.3). The method is applied for validation in Sec. 3, where the test cases are presented. Aerodynamic results are presented by comparing mid- and high-fidelity simulations with experiments, whereas for the radiated noise, the mid-fidelity solution is compared with the high-fidelity one. An isolated propeller is investigated in Sec. 3.2, whereas tandem configurations are investigated in Sec. 3.3 (co-axial configuration) and Sec. 3.4 (staggered configuration). Conclusions are presented in Sec. 4.

2. Methodology

2.1. Nonlinear vortex-lattice method

The quasi-compact aeroacoustic model used in this work is obtained by coupling the open-source DUST solver [18], an aerodynamic framework that computes the solution of a discretized lifting surface using a nonlinear vortex-lattice (NL-VL) method, and an FWH equation solver for the far-field noise propagation.

DUST relies on an integral boundary element formulation and a vortex particle model for wakes [19,20]. It implements a time-stepping algorithm, sequentially solving Morino-like problems for the potential velocity field, nonlinear problems for lifting lines, and updating the rotational velocity field by integrating the Lagrangian dynamical equations of wake particles. The code incorporates various classical aerodynamic elements, such as lifting lines, vortex lattices, and surface panels, enabling different fidelity levels in the model.

The NL-VL aerodynamic element implemented in DUST [21] results from coupling the potential unsteady vortex-lattice method with the viscous aerodynamic data provided by a tabulated coefficient. Compared to a classical lifting line, this element allows for modeling of the geometry in the chord-wise direction and extracting not only the span-wise but also the chord-wise pressure jump across the mid-plane of the blade. Moreover, the NL-VL element overcomes all numerical instability limitations of the lifting line, which is formulated as an explicit iterative problem. This aspect is fundamental for simulating aeroelastic problems with the methodology presented in [22], where a tight coupling between DUST and the multibody solver MBDyn is used for the analysis. Thus, the present framework is also suitable for assessing the effect of blade vibrations on noise generation.

The initial stage involves calculating the potential solution of the linear vortex lattice. This is achieved by solving a linear system that enforces the non-penetration boundary condition on each vortex lattice panel with normal $\hat{\boldsymbol{n}}$. The boundary condition on the k^{th} panel reads

$$\hat{\boldsymbol{n}}_k \cdot \boldsymbol{u}_{\phi,k} = \hat{\boldsymbol{n}}_k \cdot \left(\boldsymbol{v}_k - \boldsymbol{U}_\infty - \boldsymbol{u}_{\psi,k}\right), \tag{1}$$

where $\boldsymbol{u}_\phi$, $\boldsymbol{v}$, $\boldsymbol{U}_\infty$, and $\boldsymbol{u}_\psi$ are, respectively, the potential velocity, the body velocity, the free-stream velocity, and the rotational perturbation velocity vectors. In the vortex-lattice method, the surface is discretized as a sheet of vortex rings each with intensity Γ_k, equivalent to a piecewise-uniform surface doublet distribution. We introduce the influence coefficients matrix $\mathbf{A}$, where each term a_{kl} is defined as the normal velocity component induced at collocation point k by a unit-strength vortex-ring located at panel l. The unknown vortex strengths Γ_l are defined at each panel l and collected into the vector $\boldsymbol{\Gamma}$. The boundary condition is imposed for each panel collocation point k, such that

$$\sum_l a_{kl}\Gamma_l = \hat{\boldsymbol{n}}_k \cdot \boldsymbol{u}_{\phi,k} \,. \tag{2}$$

Thus, the overall vortex lattice formulation can be rewritten in a linear system form as

$$\mathbf{A}\boldsymbol{\Gamma} = \boldsymbol{b} \,, \tag{3}$$

where the right-hand side $\boldsymbol{b}$ is a vector containing the enforced boundary conditions on each panel; initially, each component corresponds to the right-hand side of Eq. (1).

Next, we define as *strip* (or *stripe*) a set of VL elements at a fixed spanwise station from the leading to the trailing edge. A fixed-point iterative problem is addressed by ensuring convergence between the lift coefficient obtained from the aerodynamic 2D look-up table and the one computed from the strip circulation. The total velocity $\boldsymbol{u}^i_{\text{sec}}$ acting on the strip control point at each time-step and iteration i can be determined as follows:

$$\boldsymbol{u}^i_{\text{sec}} = \boldsymbol{U}_\infty - \boldsymbol{v} + \boldsymbol{u}_{tot\setminus v_{nl}} + \boldsymbol{u}^{i-1}_{v_{nl}}, \tag{4}$$

where $\boldsymbol{u}_{tot\setminus v_{nl}}$ is the velocity induced by all elements except the NL-VL elements and $\boldsymbol{u}^{i-1}_{v_{nl}}$ is the velocity induced by NL-VL elements only, calculated from $\boldsymbol{\Gamma}^{i-1}$. Then, the velocity is projected on the plane formed by the strip normal $\hat{n}_{\text{sec}}$ and chord $\hat{t}_{\text{sec}}$:

$$\boldsymbol{u}^i_{2D} = \left(\boldsymbol{u}^i_{\text{sec}} \cdot \hat{\boldsymbol{n}}_{\text{sec}}\right)\hat{\boldsymbol{n}}_{\text{sec}} + \left(\boldsymbol{u}^i_{\text{sec}} \cdot \hat{\boldsymbol{t}}_{\text{sec}}\right)\hat{\boldsymbol{t}}_{\text{sec}}, \tag{5}$$

and the angle of attack of the strip is calculated as:

$$\alpha^i_{\text{sec}} = \text{atan}\left(\frac{\boldsymbol{u}^i_{2D} \cdot \hat{\boldsymbol{n}}_{\text{sec}}}{\boldsymbol{u}^i_{2D} \cdot \hat{\boldsymbol{t}}_{\text{sec}}}\right) - \frac{2\,\Gamma^{i-1}_{\text{sec}}}{C_{L/\alpha}\,\tilde{c}\,||\boldsymbol{u}^i_{2D}||}, \tag{6}$$

i.e., the geometric angle of attack corrected by taking out the velocity induced by the strip [23]. Here, $\Gamma^{i-1}_{\text{sec}}$ represents the total circulation of the strip calculated at iteration $i-1$, $C_{L/\alpha}$ denotes the slope of the lift curve in the linear range derived from tabulated data, and $\tilde{c}$ represents the chord of the strip. Thus, the viscous lift coefficient is obtained from

a 2D look-up table. For each iteration i, the vortex-lattice linear system (3) is solved by adjusting the right-hand side $\boldsymbol{b}$ according to the difference between the viscous and inviscid lift coefficient; the solution is the updated circulation. For more details on the update of $\boldsymbol{b}$, including techniques for the numerical stabilization of the method, the reader is referred to [24].

Finally, the aerodynamic load of each panel $\boldsymbol{F}_k$ is computed using the unsteady formulation of the Kutta-Joukowsky theorem, as for the linear case plus a viscous correction on the drag term $\boldsymbol{\Delta D}^{\mathrm{v}}$:

$$\boldsymbol{F}_k = \boldsymbol{F}_k^{\mathrm{sys}} + \boldsymbol{\Delta D}_k^{\mathrm{v}}, \tag{7}$$

where $\boldsymbol{F}_k^{\mathrm{sys}}$ is the force calculated from the system. The pressure jump across the k^{th} vortex-lattice panel ΔP_k is retrieved as $\Delta P_k = \boldsymbol{F}_k \cdot \hat{\boldsymbol{n}}_k / A_k$, being A_k the panel area. More details on the implementation and validation of the method can be found in [24].

To extend the limits of applicability for the described approach by improving the modeling of three-dimensional effects, a sweep correction was implemented in DUST models as proposed by Goitia and Llamas [25,26]. Nevertheless, in the present work, as the geometry of the propeller blade considered in this study is not characterized by a high sweep, this correction is not taken into account.

2.2. The acoustic problem

Noise sources are propagated to far-field observers by solving the second Kirchhoff-FWH equation proposed by Di Francescantonio [15] applied to solid surfaces, i.e., Formulation 1A by Farassat [27]. Only the terms related to the surface solutions are considered, assuming that no transonic effects occur in the class of vehicles under analysis. Thus, the quadrupole contribution is neglected. The integration is carried out on the body surface S_b. In analogy with formulation 1A, the acoustic pressure perturbation in the undisturbed medium $p' = p - p_0$ is split into its thickness p'_T and loading p'_L contributions:

$$p'(x,t) = p'_{\mathrm{T}}(x,t) + p'_{\mathrm{L}}(x,t). \tag{8}$$

By indicating the time derivative of the generic quantity X with $\dot{X}$ (i.e., with the "dot" symbol on top of it), the thickness term reads:

$$4\pi p'_T(x,t) = \underbrace{\int_{S_b} \left[\frac{\rho_0 \left(\dot{v}_i \hat{n}_i + v_i \dot{\hat{n}}_i \right)}{r|1 - M_i \hat{r}_i|^2} \right]_{\mathrm{ret}} dS}_{4\pi p'_{\mathrm{T1}}} + \underbrace{\int_{S_b} \left[\frac{\rho_0 v_i \hat{n}_i K}{r^2 |1 - M_i \hat{r}_i|^3} \right]_{\mathrm{ret}} dS}_{4\pi p'_{\mathrm{T2}}}, \tag{9}$$

whereas the loading term reads:

$$\begin{aligned} 4\pi p'_L(x,t) = & \underbrace{\frac{1}{c_0} \int_{S_b} \left[\frac{\dot{P}'_i \hat{r}_i}{r|1 - M_i \hat{r}_i|^2} \right]_{\mathrm{ret}} dS}_{4\pi p'_{\mathrm{L1}}} \\ & + \underbrace{\int_{S_b} \left[\frac{P'_i \hat{r}_i - P'_i M_i}{r^2 |1 - M_i \hat{r}_i|^2} \right]_{\mathrm{ret}} dS}_{4\pi p'_{\mathrm{L2}}} \\ & + \underbrace{\frac{1}{c_0} \int_{S_b} \left[\frac{P'_i \hat{r}_i K}{r^2 |1 - M_i \hat{r}_i|^3} \right]_{\mathrm{ret}} dS}_{4\pi p'_{\mathrm{L3}}}, \end{aligned} \tag{10}$$

where $K = \dot{M}_i \hat{r}_i r + M_i \hat{r}_i c_0 - M_i M_i c_0$, $P'_i = \left(P_{ij} - p_0 \delta_{ij} \right) \hat{n}_j$, $\hat{r}_i = r_i / r$, and $r = \sqrt{r_i r_i}$. Here, c_0 is the speed of sound in the undisturbed medium, M_i is the i^{th} component of the local Mach number vector, $\hat{n}_i$ is the i^{th} component of the surface normal vector, p_0 is the reference pressure in the undisturbed medium, P_{ij} is the fluid compressive stress tensor, r_i is the i^{th} component of the distance vector between the source and the observer, v_i is the i^{th} component of the body velocity, δ_{ij} is the Kronecker delta, and ρ_0 is the reference density. The time derivatives are calculated with respect to the retarded time $\tau = t - r/c_0$, i.e., the time at which the observer perceives the noise signal. The first term loading term, $4\pi p'_{\mathrm{L1}}$, is related to the time variation of the pressure field emitted and is here named unsteady loading. The second and the third terms, $4\pi p'_{\mathrm{L2}}$ and $4\pi p'_{\mathrm{L3}}$, are related to the pressure field and are here named steady loading. For more details, the reader is referred to the original works [15,27].

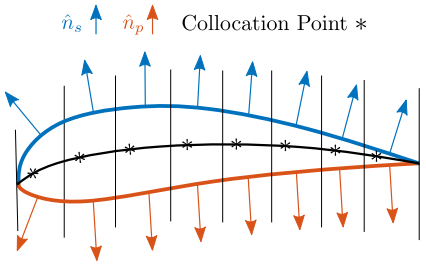

Fig. 1. Representation of the surface normal associated with each panel. The surface area is computed where the normal is defined, whereas the source-observer distance r is calculated from the collocation point (∗) on the mid-plane.

The numerical implementation has been previously validated using high-fidelity aerodynamic data computed with SU2 and comparing the radiated noise with experimental measurements [16]. In this work, we present its application to compact and quasi-compact models, particularly to acoustic sources generated with the NL-VL method.

2.3. Acoustic propagation of the mid-fidelity solution

2.3.1. Thickness noise

Thickness noise is due to the displacement of fluid mass caused by the moving object. As shown in Eq. (9), it is related to the geometry of the object and its motion, i.e., v, $\dot{v}$, $\hat{n}$, and $\dot{\hat{n}}$. As discussed by [5], airfoil thickness and chord are first-order thickness sources, whereas thickness distribution is a second-order source. A simple representation of the first-order effect of the thickness noise can be obtained by discretizing an airfoil with four points, two at the leading and trailing edges and two at the maximum thickness, to compute two surface normal vectors per airfoil side. On the other hand, the importance of thickness distribution (second-order effect) increases with increasing thickness at the leading and trailing edges.

The surface discretization of the NL-VL model allows the incorporation of first-order and second-order effects in the solution. The blade is discretized with multiple panels along its mean surface, with the collocation point located in the chord-wise direction at a quarter of each panel, towards the leading edge. The variations of the coordinates of the collocation points provide v and $\dot{v}$. The same discretization of the mean surface is applied to the thick blade to determine information about the outward-facing normal vector $\hat{n}$. The blade is split into upper and lower surfaces, and the surface normal vector of the suction and pressure sides of the blade corresponding to each vortex-lattice panel, $\hat{n}_s$ and $\hat{n}_p$, are saved for each vortex-lattice panel. Similarly, the corresponding areas on the suction and pressure sides, A_s and A_p, are assigned to the matching panel on the mean surface. These geometric quantities are shown in Fig. 1 for a 2D non-symmetric airfoil section. The only approximation introduced is the source-observer distance r, which is computed from the collocation point on the mean line. Since the thickness is much smaller than r, its effect is negligible.

2.3.2. Loading noise

Loading noise is produced by unsteady forces acting on the fluid due to the presence of the moving object. In compact formulations, the

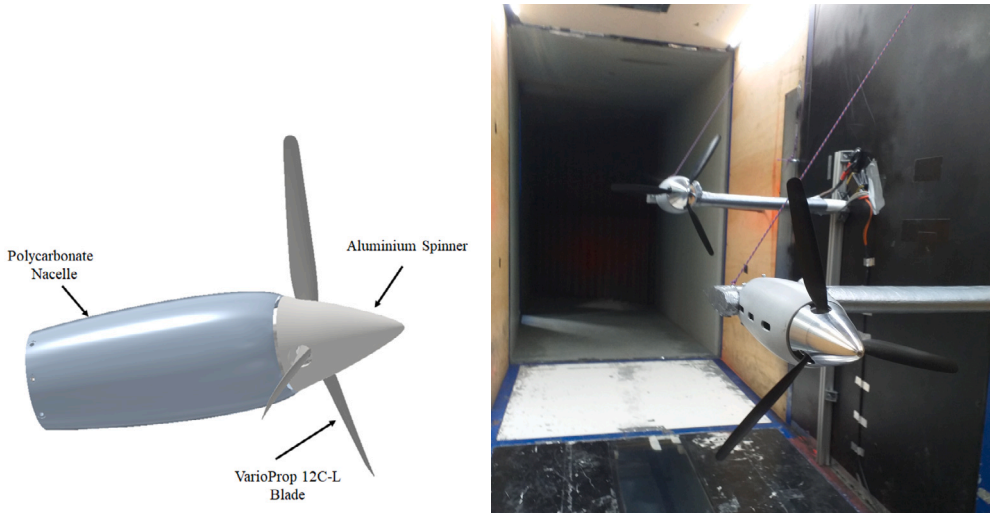

Fig. 2. (a) Layout of propeller experimental model; (b) tandem propeller models test set up at *S. De Ponte* wind tunnel [13].

chord-wise pressure distribution is replaced by the sectional lift L, and Eq. (10) is then integrated only along the span-wise direction s on the span-wise domain s_b:

$$\begin{aligned} 4\pi p'_L(x,t) = &\frac{1}{c_0}\int_{s_b}\left[\frac{\dot{L}_i\hat{r}_i}{r|1-M_i\hat{r}_i|^2}\right]_{\text{ret}} ds \\ &+\int_{s_b}\left[\frac{L_i\hat{r}_i - L_iM_i}{r^2|1-M_i\hat{r}_i|^2}\right]_{\text{ret}} ds \\ &+\frac{1}{c_0}\int_{s_b}\left[\frac{L_i\hat{r}_iK}{r^2|1-M_i\hat{r}_i|^3}\right]_{\text{ret}} ds. \end{aligned} \tag{11}$$

In this way, any information about local chord-wise pressure distribution is lost. However, this may be inevitable when aerodynamics is modelled using low-fidelity approaches where the only information available is the sectional lift.

Bernardini et al. [9] proposed reconstructing the chord-wise distribution with a superposition of shape functions using the Küssner–Schwarz general theory for thin airfoil aerodynamics. In this work, the NL-VL aerodynamic model inherently gives the chord-wise distribution of the pressure jump ΔP. Thus, the following equation is solved by integrating on the mid-plane surface S_m:

$$\begin{aligned} 4\pi p'_L(x,t) = &\frac{1}{c_0}\int_{S_m}\left[\frac{\Delta\dot{P}_i\hat{r}_i}{r|1-M_i\hat{r}_i|^2}\right]_{\text{ret}} dS \\ &+\int_{S_m}\left[\frac{\Delta P_i\hat{r}_i - \Delta P_iM_i}{r^2|1-M_i\hat{r}_i|^2}\right]_{\text{ret}} dS \\ &+\frac{1}{c_0}\int_{S_m}\left[\frac{\Delta P_i\hat{r}_iK}{r^2|1-M_i\hat{r}_i|^3}\right]_{\text{ret}} dS, \end{aligned} \tag{12}$$

where $\Delta P_i = \Delta P\hat{n}_i$. If only one panel is used for the chord-wise discretization, the NL-VL model collapses to an implicit lifting-line model, and the compact model given by Eq. (11) is retrieved. According to the configuration under analysis, when compact model assumptions fail, i.e., when the chord length is not negligible with respect to the source–observer distance or there are high chord-wise pressure gradients, it is still possible to obtain a converged solution by increasing the number of panels in the chord-wise direction.

3. Results and discussion

The activity aims to validate and characterize the capabilities of the reduced-order model for acoustic evaluation, compared to a higher-fidelity computational fluid dynamics (CFD) solution coupled with the same FWH solver. This validation process involves a set of test cases to tackle different physical aspects and increasingly difficult scenarios of propeller noise generation. In particular, the selected test cases reproduce the experimental activity performed in the S. De Ponte wind tunnel of Politecnico di Milano over two scaled propeller models in tandem configuration. The experimental dataset does not include acoustic data because the tests were not performed in an anechoic wind tunnel. In detail, a three-bladed propeller with a diameter $D = 0.3\,\text{m}$ has been simulated. In particular, left-handed VarioProp 12C blades were used, with pitch angle β at $0.75R$ set to 26.5°. This particular blade configuration proves challenging due to each blade section's high relative incidence angle. Viscous effects are relevant, and the NL-VL model can be validated thoroughly. A spinner and a nacelle complete the layout of the propeller model (see Fig. 2(a)) used in the experiments to shield the embedded motor and load cell. Two twin propeller models were mounted in the wind tunnel to study the aerodynamic interaction effects between tandem propellers in cruise flight, reproducing different degrees of overlap between the rotor disks. The tandem propeller models inside the wind tunnel test section are shown in Fig. 2(b). More details on the experiments are available in [13].

In the following subsections, three different test cases are investigated numerically for the scope of the present work: first, an isolated propeller in forward flight is considered; then, tandem co-axial and staggered configurations are examined. The rotors are co-rotating in the tandem cases. The azimuthal angle of the blades of the two rotors is equal in the simulations, whereas the phase of the rotors was not synchronized in the experiments, despite both operating at the same nominal rotational speed. Table 1 reports the parameters of the test conditions under analysis. Fig. 3 shows a schematic representation of the two propeller positions, where the axial distance L_x and the lateral separation L_y are expressed in terms of the propeller radius $R = 0.15\,\text{m}$.

DUST numerical models of the propeller were created by using a 3D scan of the blade and the CAD drawing of the spinner-nacelle system. Airfoil sections, twist, dihedral angle, and chord distributions along the blade radial coordinate used for the numerical models are reported in [28]. The 2D aerodynamic coefficients of the selected airfoils required for viscous corrections in blade modelling were calculated by

Table 1
Summary of the test conditions.

Quantity	Symbol	Value	Unit
Advance ratio	J	0.8	-
Rotational speed	Ω	7050	RPM
Pitch angle at $0.75R$	β	26.5	°
Freestream Temperature	$\mathcal{T}_\infty$	294.05	K
Freestream Density	ρ_∞	1.18	kg/m^3
Rotor Radius	R	0.15	m
Axial separation	L_x/R	5	-
Lateral separation	L_y/R	0 - 1	-

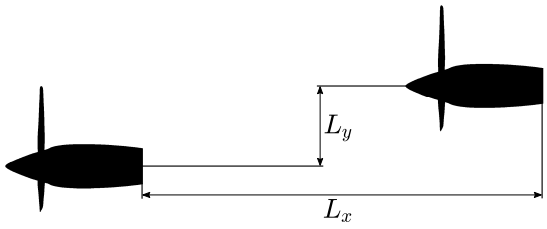

Fig. 3. Schematic representation of the propeller layout.

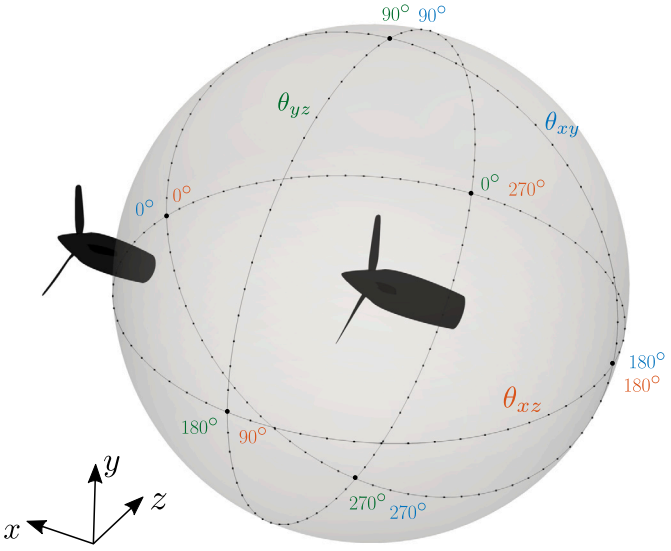

Fig. 4. Schematic representation of the observer locations. The observers are located at a distance $5R$ from the center of the propeller disk.

XFOIL simulations [29] in the range of angles of attack before stall. The Viterna method [30] was used to calculate the post-stall behavior of the sectional aerodynamic load coefficients in the angle of attack range between ±180°. The complete geometry of the propeller model is open and will be provided by the authors upon request.

In the following, the experimental integral loads of the propellers in terms of thrust (C_T) and power (C_P) coefficient are first considered for the validation of the numerical aerodynamic models. Then, the attention is focused on acoustic evaluation. Fig. 4 shows a schematic representation of the observers considered. Two sets of observers have been defined on a sphere of radius $5R$ centered in the center of the (rear, if tandem) propeller disk by cutting it with two perpendicular planes. Plane yz lies on the propeller disk, and plane xy is the axial and lateral separation plane. Plane xz, orthogonal to the previous ones, is ignored since it would carry the same information as plane xy for the axial configurations. The spinner and the nacelle are not included as a noise source for all configurations, although they contribute to generating the flow field. Only the rear propeller is considered a noise source for tandem configurations since the most relevant phenomena are confined to it. Acoustic data are compared in terms of both pressure fluctuation (p', Pa) time series and sound pressure level (SPL, dB) defined as

$$\mathrm{SPL}_{\square} = 20 \cdot \log_{10} \frac{\mathrm{rms}(p'_{\square} - E(p'_{\square}))}{p_{\mathrm{ref}}}, \tag{13}$$

where $p_{\mathrm{ref}} = 20\,\mu\mathrm{Pa}$ is the reference pressure, $E()$ is the expected value of the signal, and $_{\square}$ can be replaced by $_{\mathrm{T}}$ or $_{\mathrm{L}}$ whether thickness or loading contributes are considered, according to Eq. (9)–(10). When omitted, $p'(t)$ from Eq. (8) will be considered, and the quantity will be referred to as Overall Sound Pressure Level (OASPL). For the staggered configuration, the tonal contribution of the SPL up to the third blade passing frequency has been computed. The procedure considers the pressure fluctuation signal and applies a second-order Butterworth bandpass filter, as suggested in [31], with a band of ±50 Hz. The filtered signal is then used for the computation of the $\mathrm{SPL}_{\mathrm{BPF}}$ following Eq. (13).

3.1. Numerical modelling

The primary objective of this study is to compare the NL-VL model with a lifting line (LL) model in terms of noise emissions, i.e., using quasi-compact and compact noise sources. The LL model is created by considering a single panel in the chord-wise direction. In contrast, the NL-VL chord-wise discretization is built using 5 collocation points, having evaluated convergence on both integral loads and SPL. For brevity, results obtained with 10 collocation points in the chord-wise directions used to evaluate convergence will be generally omitted unless otherwise specified. A span-wise discretization of 50 elements for each propeller blade is considered for both models. DUST simulations span 10 rotor revolutions with a time discretization equivalent to 5 °/iter of blade azimuthal angle. Spatial and time discretization parameters are coherent with the best practices assessed in previous studies on this propeller configuration [13,28]. Concerning the LL model, the far-field propagation of the surface pressure fluctuations yields the application of a compact model. For this configuration, since the projection of the collocation point on the pressure and suction side, according to Fig. 1, results in opposite normals, the overall thickness contribution cancels out and it is therefore discarded in part of the following comparisons.

3.1.1. Reference solution

The reference aeroacoustic solutions are generated by computing the pressure perturbation at the observer locations with the FWH solver, given the aerodynamic input computed with the unsteady Reynolds Averaged Navier-Stokes uRANS solver SU2. SU2 [32] is an open-source software developed for solving partial differential equations, focusing on computational fluid dynamics. In this work, a steady RANS simulation in a rotating reference frame (RRF) approach [33] is used for the single propeller and the tandem co-axial configurations. Fully unsteady simulations applying a sliding mesh technique (SM) [34,35] are used to solve the aerodynamic field for the tandem configurations. This approach is necessary when dealing with complex scenarios, such as non-axial flight conditions and multiple propellers with arbitrarily relative positions. Among the several options offered within SU2, the central Jameson-Schimdt-Turkel (JST) scheme for convective fluxes discretization has been applied in all the computations [36]. Turbulence has been modeled with the Spalart-Allmaras (SA) model [37]. Concerning the steady simulations, the standard SA is modified by the algebraic BCM transition model from [38]. In the case of unsteady simulations, a second-order dual time-stepping method is used, and the time-step is fixed to achieve 1 °/iter.

To ensure the accuracy of the reference data, the independence of the solution on spatial discretization is investigated by comparing three different grid resolutions. All grids are characterized by a y^+ value of 1 at the wall to operate within the hypotheses of the turbulence model. The coarsest grid has fewer surface points and a coarser wake discretization than the others. In the isolated test case, the medium and fine grids are generated using a linear grid refinement factor of 1.4 on surface and volume cells. It will be shown that the medium grid achieves good

Table 2
Grid cell count for the RANS and uRANS simulations.

Grid	Isolated propeller	Staggered propellers
Coarse	6.9×10^6	19.3×10^6
Medium	18.0×10^6	44.3×10^6
Fine	56.6×10^6	72.2×10^6

Table 3
Convergence of thrust and power coefficients for the RANS simulations (isolated test case).

Grid	C_T	C_P
Coarse	0.096	0.110
Medium	0.102	0.114
Fine	0.102	0.114
Experimental	0.100	0.112

Table 4
Convergence of average thrust and power coefficients and PSD S_{xx} of the thrust coefficient at the 1^{st} bpf of the rear propeller for the uRANS simulations ($L_y/R = 1$). The PSD value is integrated in a band of ±50 Hz width centered at the peak.

Grid	C_T	C_P	$S_{xx}(1^{st}$ BPF)
Coarse	0.1078	0.1249	0.0166
Medium	0.1093	0.1252	0.0143
Fine	0.1076	0.1235	0.0113
Experimental	0.1010	0.1107	0.0095

grid convergence. Thus, in the tandem test case with axial separation, the medium grid is generated with the same criteria as the isolated test case. From this, the fine grid is refined only in the propeller wake region. Table 2 reports the grid cell count of the isolated and tandem test case.

Convergence is reached with respect to the integral aerodynamic loads as shown in Tables 3 and 4. In particular, for the staggered case, limited ($< 2\%$) variations of the coefficients are found, although with no clear convergence trend. However, the most refined grid better captures the thrust fluctuations at the blade passing frequency (BPF) when compared to the experimental data. This is shown by reporting the value of the power spectral density (PSD) S_{xx} of the thrust coefficient at that frequency. Thus, the finest grid will be used as a reference in the staggered test case. The behavior will be further investigated in the following.

Table 5
Average relative difference over all the observer locations considered for the RANS computations. (C: coarse, M: medium, F: fine).

	Isolated propeller [dB]	Staggered propellers [dB]
Δ_{C-F}	0.470	1.11
Δ_{M-F}	0.064	0.61

Table 6
Thrust and power coefficients evaluated for the isolated propeller by the different computational methods.

Solution	C_T	C_P
LL	0.118	0.115
NL-VL	0.103	0.107
RANS	0.102	0.114
Experimental	0.100	0.112

To evaluate convergence in terms of the acoustic results, a difference of the OASPL, defined in Equation (14), is computed between the finest grid and the coarse and medium results:

$$\Delta^i_{A-B} = |\mathrm{OASPL}^i_A - \mathrm{OASPL}^i_B|, \tag{14}$$

where the index i denotes i^{th} observer location.

Fig. 5 shows the relative difference of the OASPL over the propeller plane. Averaged values for the isolated and the staggered test cases are reported in Table 5. The trends observed for the aerodynamic loads are confirmed. Thus, the medium grid will be used as the reference for the isolated propeller. For the tandem staggered configuration, the fine grid will be used since the relative error of the medium grid is not limited to all observers.

3.2. Isolated propeller

The first test case examined is the isolated propeller in forward flight. This sets a benchmark for the subsequent configurations and allows a direct comparison with experimental aerodynamic data. Also, the test case is used to assess the aeroacoustic solver's capability to handle different aerodynamic solutions provided as input. Table 6 compares computational and experimental data loads. The NL-VL model is more accurate than LL, particularly considering the thrust coefficient.

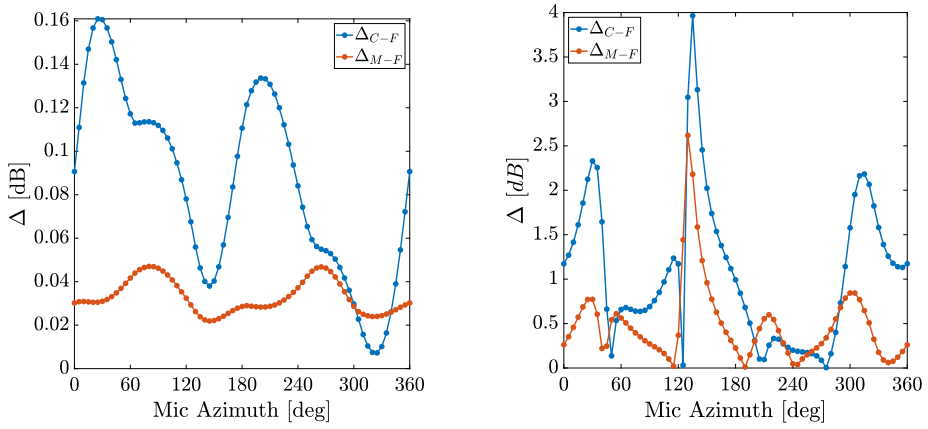

(a) Isolated propeller. (b) Staggered propellers.

Fig. 5. Relative difference of the OASPL over the propeller plane, (θ_{yz}). Line C-F is the relative error between coarse and fine grid, line M-F between medium and fine grid.

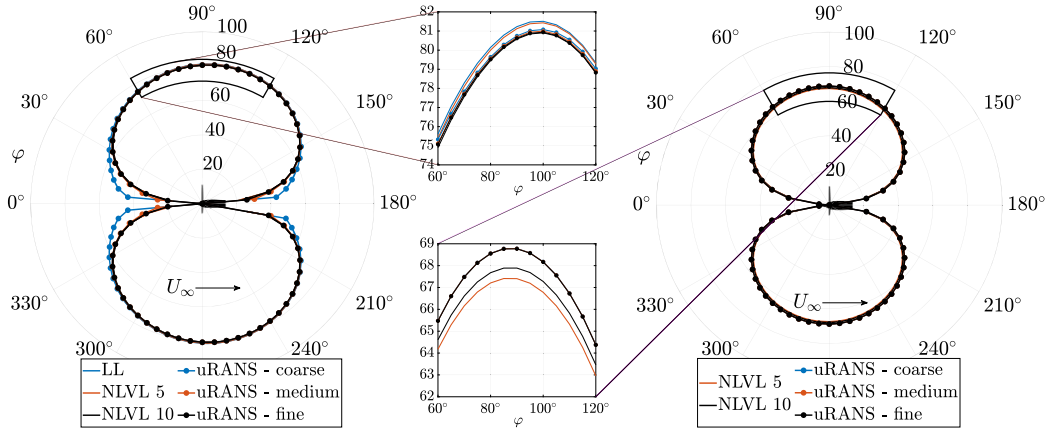

(a) Loading noise SPL_L. (b) Thickness noise SPL_T.

Fig. 6. Directivity comparison of the single propeller configuration for different methods in the lateral plane (xy).

Table 7
Thrust and Power coefficients evaluated for the rear propeller in co-axial configuration ($\frac{L_x}{R} = 5$ and $\frac{L_y}{R} = 0$) by the different computational methods.

Solution	C_T	C_P
LL	0.0646	0.0680
NL-VL	0.0637	0.0641
RANS (RRF)	0.0701	0.0917
uRANS	0.0730	0.0947
Experimental	0.0725	0.0895

Figs. 6(a) and 6(b) show a comparison of the loading and thickness noise contributions for the different methods in the lateral plane xy, respectively. For this test case, the results with all the discretizations are reported. The number next to "NLVL" indicates the number of chord-wise elements used in the NL-VL simulations. For the high-fidelity simulations, the lines are indistinguishable; indeed, the relative error on the OASPL is always lower than 0.2%, as presented earlier in Fig. 5(a). The mid-fidelity methods accurately evaluate the acoustic signature of this propeller configuration. Overall, the loading noise gives the highest contribution, which will also be dominant in the subsequent investigated test cases. Differences in loading noise (Fig. 6(a)) between the compact and quasi-compact solutions cannot be appreciated – the test case lies within the assumptions of acoustic compactness. On the other hand, minor differences (< 1 dB) are present in thickness noise (Fig. 6(b)) when increasing the chord-wise resolution in the quasi-compact model.

3.3. Tandem propellers: co-axial configuration

The second test case studied is the co-axial co-rotating tandem configuration. The relative position of the two propellers is coherent with Fig. 3, where $\frac{L_x}{R} = 5$ and $\frac{L_y}{R} = 0$. This specific test case directly compares all the computational approaches in a context where aerodynamic interaction effects on the rear propeller are relevant. Table 7 shows the rear propeller's average thrust and power coefficient compared to experimental values. As previously shown in [13], this specific configuration is characterized by a load reduction of the rear propeller, with respect to the single propeller configuration, that is constant in time and independent from the blade azimuthal position. The RANS (in a rotating reference frame) and uRANS (with sliding mesh) solutions agree with experimental data, while mid-fidelity methods show a more significant discrepancy in both load coefficients.

The loading contribution to the SPL obtained with the different aerodynamic solutions is shown and compared in Fig. 7(a) for the lateral plane and Fig. 7(b) for the propeller plane. Changing the reference solution from RANS to uRANS introduces little variation in the SPL everywhere except for the region around the propeller axis, where the loading contribution of the steady solution tends to zero, whereas the unsteady solution generates unsteady loading noise sources. The difference in the rotor plane between the quasi-compact and the compact solution is minimal (Fig. 7(b)). The uRANS and the quasi-compact solutions show an excellent agreement everywhere, including the region close to the propeller axis (Fig. 7(a)). On the other hand, the compact solution provides a significant overestimation of the SPL_L in that region, meaning that the contribution to unsteady loading provided by the compact solution is larger. Notably, all the unsteady solutions provide a slightly asymmetric solution on the propeller plane. The amount of the asymmetry is directly linked to the magnitude of the pressure variations during the rotor revolution, which is maximum considering the compact solution, and would disappear by considering the average pressure of the input signal. Overall, the results are satisfactory, with a maximum difference between the NL-VL quasi-compact method and the uRANS computation of 3.5 dB on the loading component close to the propeller axis. On average, the difference between the quasi-compact method and the uRANS computation is 1.3 dB.

3.4. Tandem propellers: staggered configuration

The final test case considered is a tandem staggered configuration, where the propellers are positioned at $\frac{L_x}{R} = 5$ and $\frac{L_y}{R} = 1$ in the test conditions defined in Table 1. This particular configuration is selected because of the high unsteadiness of the loads acting on the rear propeller. The interaction of the front propeller slipstream strongly affects the rear propeller performance, as shown by the experimental activity in [13]. Table 8 reports the values of the averaged aerodynamic load coefficients evaluated for the rear propeller in both experiments and simulations.

Similarly to the co-axial configuration, the uRANS solution agrees with experiments with a slight overestimation of the load coefficients. On the other hand, both LL and NL-VL methods slightly underestimate the thrust and power coefficients of the rear propeller. In particular, the time histories of the rear propeller thrust computed using the different methods over the last two revolutions are shown in Fig. 8. Both methods capture the periodicity of the thrust coefficient fluctuations at the blade passing frequency. This phenomenon is due to the impingement of the wake generated by the front propeller and its vortices on the rear propeller blades. Indeed, the uRANS result shows the presence of a secondary oscillation in the load signal with lower amplitude (before the

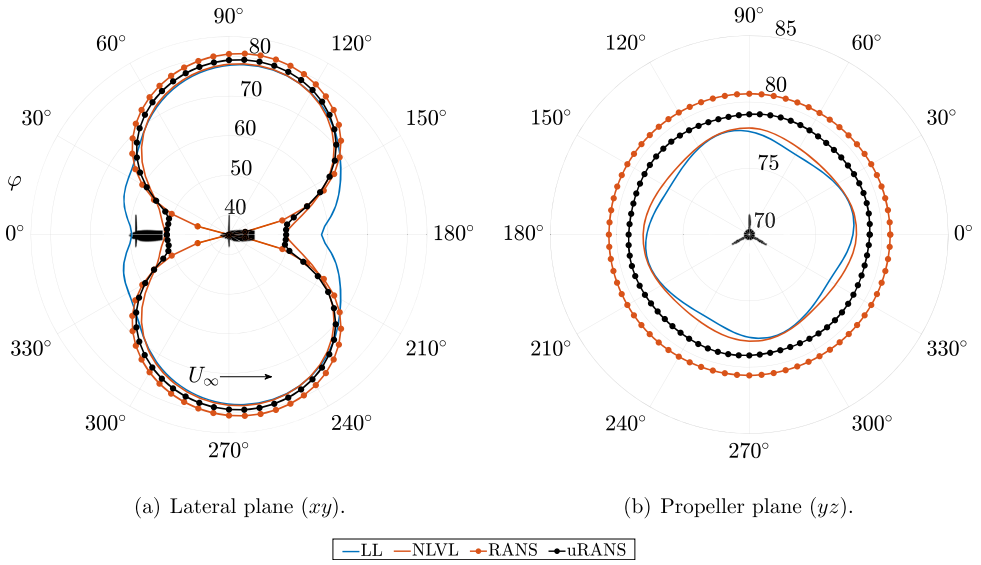

(a) Lateral plane (xy). (b) Propeller plane (yz).

Fig. 7. Loading noise SPL_L directivity comparison of the tandem co-axial configuration for different methods.

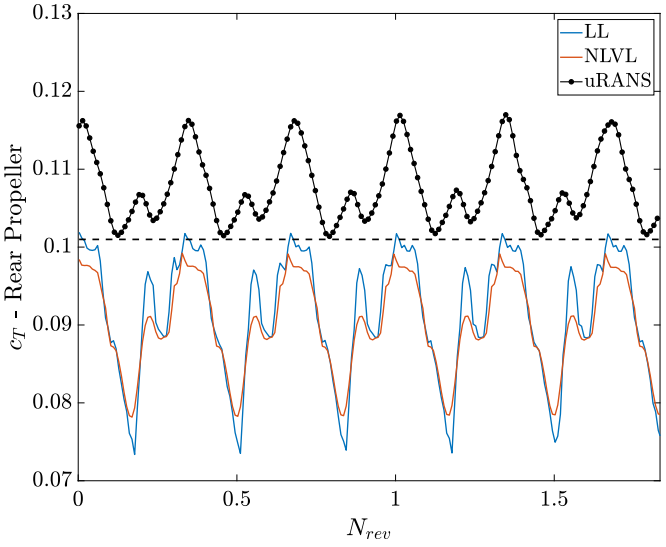

Fig. 8. Thrust coefficient C_T time histories of the rear propeller in the staggered configuration ($\frac{L_x}{R} = 5$ and $\frac{L_y}{R} = 1$). The dashed line shows the average value of the experimental data.

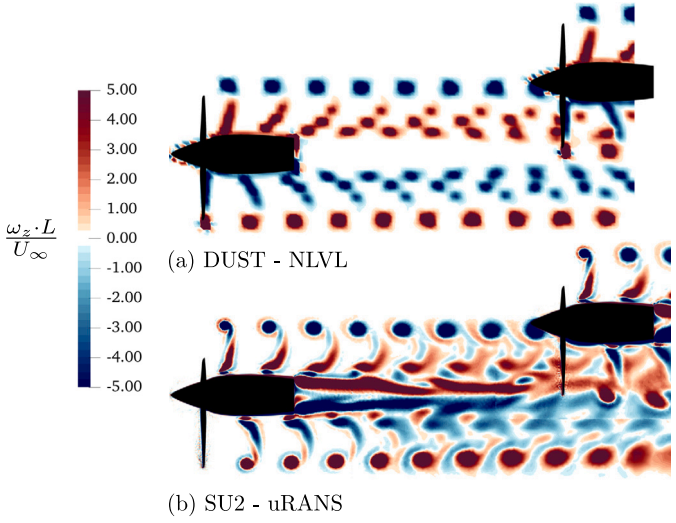

Fig. 9. Comparison of the z-component vorticity in the lateral plane xy for the staggered configuration ($\frac{L_x}{R} = 5$ and $\frac{L_y}{R} = 1$).

Table 8
Thrust and Power coefficients evaluated for the rear propeller in the staggered configuration ($\frac{L_x}{R} = 5$ and $\frac{L_y}{R} = 1$) by the different computational methods.

Solution	C_T	C_P	$S_{xx}(1^{st}$ BPF)
LL	0.0901	0.0849	0.0194
NL-VL	0.0900	0.0903	0.0159
uRANS	0.1076	0.1235	0.0113
Experimental	0.1010	0.1107	0.0095

maximum) and a secondary inflection after the maximum. The contribution of this secondary peak captured by the NL-VL model matches the high-fidelity solution more accurately. The oscillating unsteady behavior of the rear propeller load distribution directly affects noise emission.

Fig. 9 shows a comparison of the uRANS and NL-VL solutions in terms of the out-of-plane z-component vorticity field along the lateral plane xy. Further comparisons are shown in Figs. 10 and 11, where a three-dimensional visualization of vorticity magnitude iso-surfaces and the x-component vorticity field in the propeller disk plane are reported. The uRANS solution captures additional vortical structures detaching from the front propeller, i.e., a counter-rotating vortex generated from the interaction of the blade root vorticity and the stationary nacelle, and the wake of the nacelle itself, which interact as they are convected downstream to the rear propeller. Following the path of a blade of the rear propeller, the maximum thrust shown in Fig. 8 occurs when its tip is located in the wake of the bluff body at an azimuthal angle $\psi \sim 180°$. The inflection occurs slightly later, at $\psi \sim 200°$, when the blade interacts with the vortical wake released from the span of a blade of the front propeller. Finally, the secondary maximum occurs when the tip vortex of the front propeller is impinging the blade's root exiting the wake region at $\psi \sim 250°$. These result in two separate phase shifted contributions at the first BPF.

The mid-fidelity solution correctly captures the phenomena depicted above, except for the nacelle wake. Indeed, the potential approach can describe only limited physics of bluff-body aerodynamics. The vortical

(a) DUST - NLVL (b) SU2 - uRANS

Fig. 10. Comparison of the vorticity magnitude iso-surfaces colored by x-component vorticity for the staggered configuration ($\frac{L_x}{R} = 5$ and $\frac{L_y}{R} = 1$).

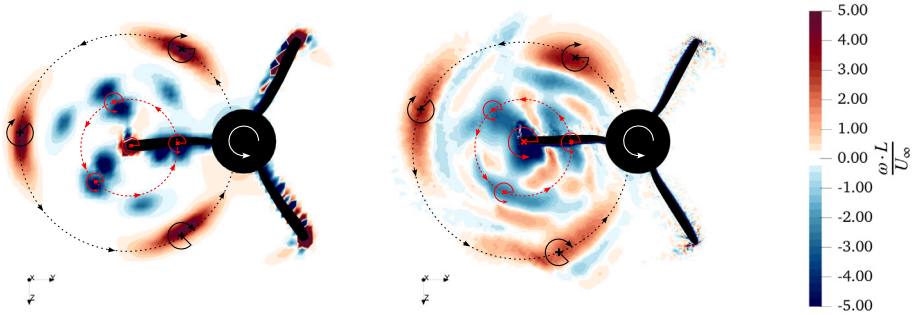

(a) DUST - NLVL (b) SU2 - uRANS

Fig. 11. Comparison of the x-component vorticity in the propeller plane (θ_{yz}) for the staggered configuration ($\frac{L_x}{R} = 5$ and $\frac{L_y}{R} = 1$).

contributions previously described directly impact the rear propeller at different portions of the blade. The quantitative visualizations of the footprints of the vortices shown in Figs. 9 to 11 demonstrate the similarities and differences between the two approaches.

Considering the acoustic evaluation, a detailed analysis of the rear propeller on both the disk and lateral planes is provided hereafter. As previously noted, the dominant noise contribution for this test case is connected to the unsteady loading of the rear propeller. Fig. 12 shows the directivity plot of the loading noise contribution in the rear propeller plane yz, and the contribution associated with the first three BPF. Results show a significant difference in noise directivity as well as a noise increase in many propagation directions with respect to the co-axial configuration, where the SPL is ~ 80 dB at all azimuthal positions. The increased noise level for the staggered configuration is in accordance with the load spectral analysis of the rear propeller measured during the experimental campaign [13].

The quasi-compact model (NL-VL) captures a loading noise directivity closer to the reference computation. The differences between the compact and the quasi-compact formulations observed in the global SPL_L arise both from the 1^{st} and the 2^{nd} BPF. Indeed, the contribution of the 2^{nd} BPF is comparable to or even greater than that of the 1^{st} BPF, specifically in the range $\theta_{yz} \in [210°, 330°]$. This occurs when the rear propeller is positioned within the wake of the front one, and with higher intensity, the source motion is directed toward the observer. The most significant differences between the two formulations are present at the 2^{nd} BPF and are related to the unsteady load variation, as shown below.

An alternative analysis of the loading noise contribution is provided by Fig. 13, where a linear plot of SPL_{L1}, SPL_{L2}, and SPL_{L3} are shown along with the pressure fluctuations of the steady and unsteady loading terms p'_{L1}, p'_{L2}, and p'_{L3}, as previously defined in Eq. (12). The first term, p'_{L1}, is related to the time derivative of the pressure jump across the surface ΔP, whereas p'_{L2} and p'_{L3} are related to the pressure jump itself ΔP. Given that the largest overall contribution is due to p'_{L1}, unsteady loading on the blade is the dominant noise source. The proposed NL-VL model proves its advantage over the lifting line solution. Indeed, when analyzing each term separately, the chord-wise spatial refinement shows a significant difference for the p'_{L1} component. This term has non-negligible contributions at frequencies higher than the BPF. In contrast, for the p'_{L2} and p'_{L3} terms, the difference is minor, and the dominant signal is at the first BPF. Further refining the chord-wise discretization led to negligible differences, meaning that a converged solution was reached. In the NL-VL solution, this improvement can be partially explained by considering that, with a higher number of elements along the chord direction, the pressure over the blade surface is locally distributed in space. Indeed, the NL-VL method can compute a local angle of attack along the chord depending on the distance with the vortex particles. As a result, when computing the noise propagation, the acoustic pressure peak is likewise more distributed in time. It is worth noticing that the greatest difference in p'_{L1} with the high-fidelity solution is at $\theta_{yz} \sim 120°$, where the relative error of the reference solution was maximum (see Fig. 5(b)). Less diffusive grids increased the SPL in that region.

Considering the lateral planes xy and xz, Fig. 14 shows the directivity of the SPL_L loading contribution computed with the different methods, together with the first and second blade passing frequencies. The aerodynamic interaction phenomena previously described significantly increase the noise contribution. Indeed, the directivity of the loading component changes significantly compared to the isolated and the co-axial configurations at these locations. On these planes, the differences observed between the quasi-compact and compact formulations are smaller. Once again, the most noticeable differences are found at the 2^{nd} BPF. The SPL_L in the two planes is similar in magnitude and directivity, primarily due to the contribution of the 1^{st} and 2^{nd} BPF. However, the directivity of the BPF differs between the two planes, be-

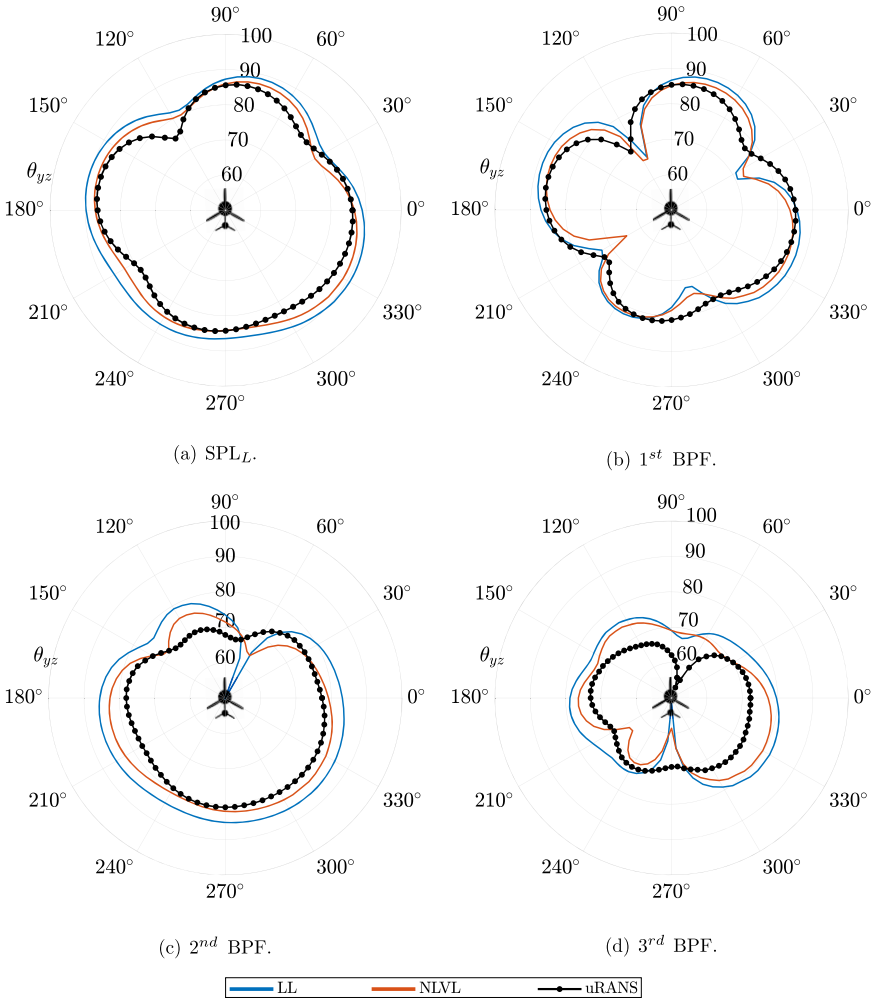

(a) SPL_L. (b) 1^{st} BPF. (c) 2^{nd} BPF. (d) 3^{rd} BPF.

Fig. 12. Loading term contribution to the SPL in the yz plane for the rear propeller: overall SPL_L and SPL_L at the first three BPF. The set of observers ($r = 5R$) is defined in Fig. 4.

ing more symmetrical in the xy plane and highly asymmetrical in the xz plane. These symmetries and asymmetries are related to the alignment and misalignment of the local source motion with the radiation direction; this modulates the intensity of the source. In the xz plane, the 1^{st} BPF primarily acts on ($\theta_{xz} \in [0°, 180°]$) with stronger emission from the region with no interaction effects and where the propeller is generating thrust. In contrast, the 2^{nd} BPF is mostly characterized by noise in ($\theta_{xz} \in [180°, 360°]$) with dominant sources originating from the region where the blade interacts with the wake of the front propeller. When the 2^{nd} BPF is comparable to or greater than the 1^{st} one, since the differences between the compact and the quasi-compact formulations are more significant at this harmonic, the effect on the global SPL_L is more evident.

More in detail, Fig. 15 shows the time histories of the pressure fluctuations for a single blade of the rear propeller evaluated by an observer at $\theta_{xy} = 180°$ in the lateral plane. Similarly to the previous plane, the noise signal is almost entirely generated by the pressure peak due to the unsteady loading contribution. A comparison of the pressure fluctuations signals shows that the mid-fidelity computations are similar and reproduce the behavior of the uRANS solution with a slight overestimation of the peak. As previously discussed, an increased number of elements in the chord-wise direction generates a reduction of the pressure peaks perceived at the observer location. The NLVL solution with 10 points discretization in the chordwise direction is also included to show the convergence in time of the perceived acoustic signal. Although differences are generally limited, by using the proposed model, it is possible to guarantee the convergence not only of the aerodynamic solution but also of the noise radiation with respect to the chord-wise discretization of the blade.

The computational cost required to compute the flow-field in the tandem test-cases is about 10 minutes for the LL discretization and 20 minutes for the NL-VL discretization, using a workstation with a Dual IntelRXeon Gold 6230R @2.10 GHz processor with 52 physical cores and 2 threads for each core [24]. The increase in computational cost is considered a fair trade-off with the ability to obtain converged aero-acoustics solutions, especially if compared with the high-fidelity URANS prediction. When the acoustic module is executed on a single core, considering both propellers and all observer locations, the compact formulation is solved in 106 seconds and the quasi-compact in 149 seconds, resulting in a negligible increase in CPU time.

4. Conclusions

In this paper, we have introduced a quasi-compact non-linear vortex-lattice formulation for tonal noise predictions to address the issue of using compact acoustic models outside their range of applicability. The model has been applied to a multirotor configuration where interaction effects are relevant. The quasi-compact model is based on the non-linear vortex-lattice method coupled with a Ffowcs-Williams Hawkings solver for aerodynamic computations and solid-surface noise radiation. The model collapses to a compact model when a single vortex lattice panel is used in the chord-wise direction. One of the key advantages

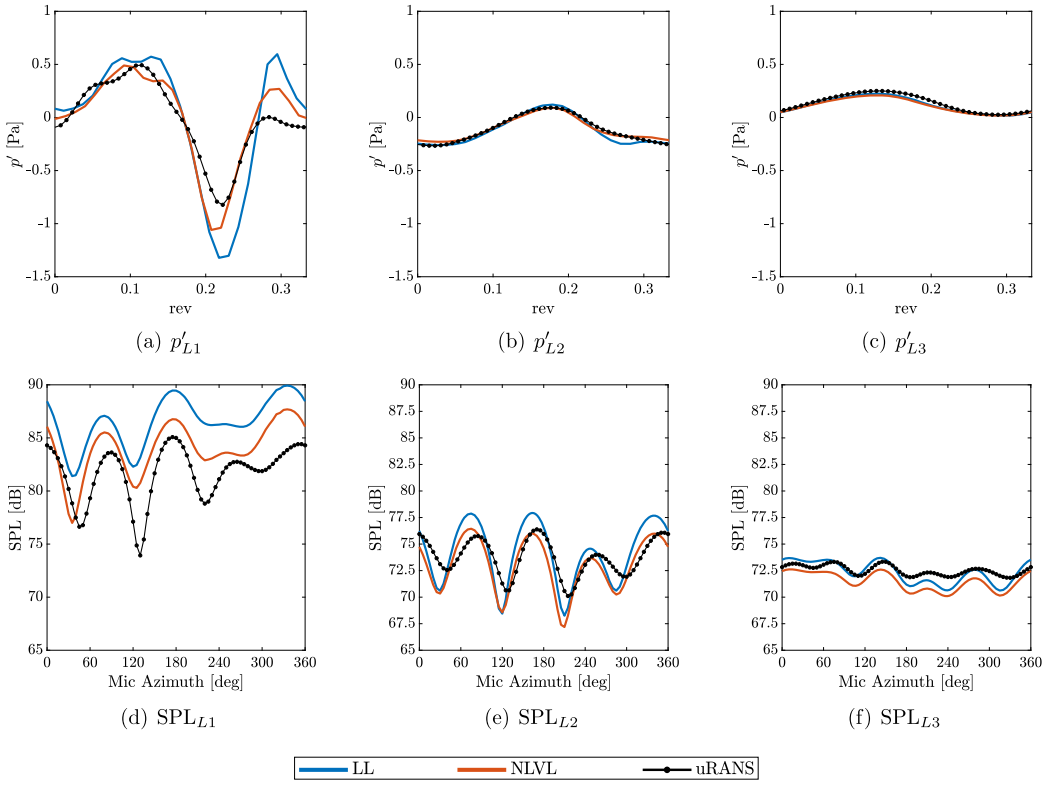

Fig. 13. Loading term decomposition for the rear propeller in the staggered configuration ($\frac{L_x}{R} = 5$ and $\frac{L_y}{R} = 1$). First row: pressure fluctuation of Observer at $\theta_{yz} = 180°$. Second row: SPL_L in the yz plane. The set of observers ($r = 5R$) is defined in Fig. 4.

of this model is its ability to represent non-linear aerodynamics accurately while keeping computational costs low, similar to lifting lines. In addition, it provides valuable information regarding the pressure jump distribution across the chord-wise direction. We demonstrate that this additional information does not provide any significant change in SPL estimation when the assumptions for compact propagation are valid. In such cases, the compact model already provides a converged solution, e.g., for an isolated rotor in axial flight. However, it is necessary to model correctly the unsteady loading arising from propeller-wake interaction.

The model presented provides specific advantages as opposed to classic compact formulations. First, depending on the test case under analysis, it is possible to find the chord-wise discretization which guarantees the convergence of the method in terms of far-field acoustic noise emission, both for thickness and loading components. Second, second-order effects of the thickness noise contribution can be captured. And third, a better evaluation of the loading contribution is achieved, specifically for configurations characterized by complex blade-vortex interactions, such as staggered propellers. In detail, the converged solution of the quasi-compact formulation predicts unsteady loading effects generated by wake- and blade-vortex interaction phenomena with greater accuracy than the compact model counterpart when compared to high-fidelity uRANS solutions. As a result, the greatest differences between the quasi-compact and the compact formulations are found in the contribution of the loading term depending on the time derivative of the pressure jump $\dot{\Delta P}$. Furthermore, this discrepancy is more evident in noise associated with the 2^{nd} BPF, which may become of the same magnitude or higher than the 1^{st} one.

The mid-fidelity methods described in this work accurately compute the tonal acoustic solution in complex interacting propeller configurations. The level of accuracy in terms of overall noise directivity is comparable to high-fidelity uRANS results, yet with a lower computational cost. A primary drawback is related to the accurate prediction of bluff bodies due to potential method limitations. Overall, the proposed method is suitable for the computation of acoustic signatures, which can be used in the preliminary design of electrically distributed propulsion vehicles.

CRediT authorship contribution statement

F. Caccia: Writing – review & editing, Validation, Conceptualization, Methodology, Writing – original draft, Investigation, Formal analysis, Project administration. **L. Galimberti:** Writing – review & editing, Validation, Formal analysis, Writing – original draft, Investigation, Data curation, Visualization. **L. Abergo:** Validation, Software, Investigation, Writing – review & editing, Methodology, Conceptualization. **A. Savino:** Validation, Methodology, Software, Investigation, Data curation, Formal analysis. **A. Zanotti:** Supervision, Project administration, Funding acquisition, Investigation, Conceptualization, Writing – review & editing, Resources. **M. Parsani:** Resources, Writing – review & editing, Funding acquisition, Supervision. **A. Guardone:** Resources, Supervision, Project administration, Conceptualization, Funding acquisition.

Declaration of competing interest

The authors declare that they have no known competing financial interests or personal relationships that could have appeared to influence the work reported in this paper.

Acknowledgements

The authors gratefully acknowledge the HPC resources provided for this collaborative effort by the Supercomputing Laboratory at King Abdullah University of Science & Technology (KAUST) in Thuwal, Saudi Arabia.

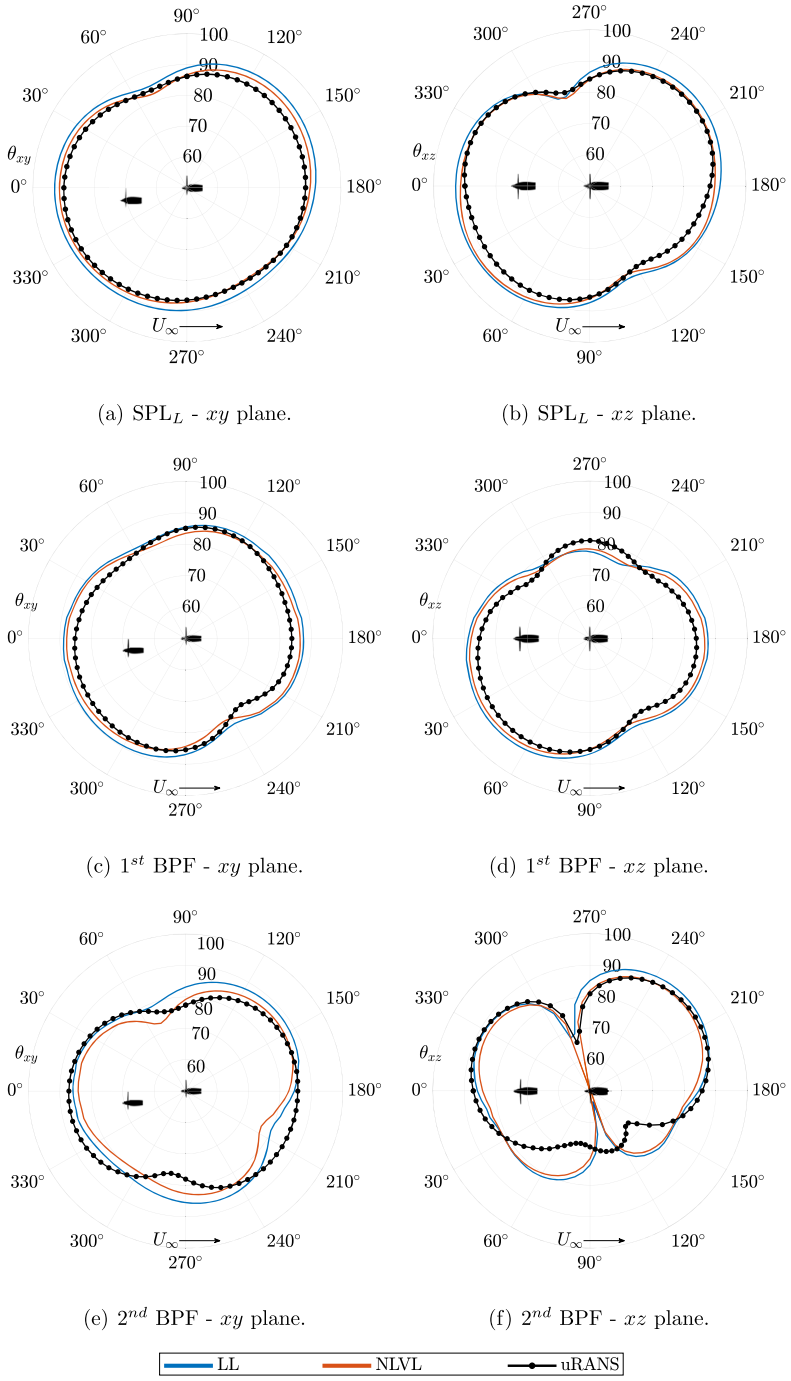

(a) SPL_L - xy plane.

(b) SPL_L - xz plane.

(c) 1^{st} BPF - xy plane.

(d) 1^{st} BPF - xz plane.

(e) 2^{nd} BPF - xy plane.

(f) 2^{nd} BPF - xz plane.

Fig. 14. Loading term contribution to the SPL in the xy (left) and xz (right) planes for the rear propeller: overall SPL_L and SPL_L at the first two BPF. The set of observers ($r = 5R$) is defined in Fig. 4.

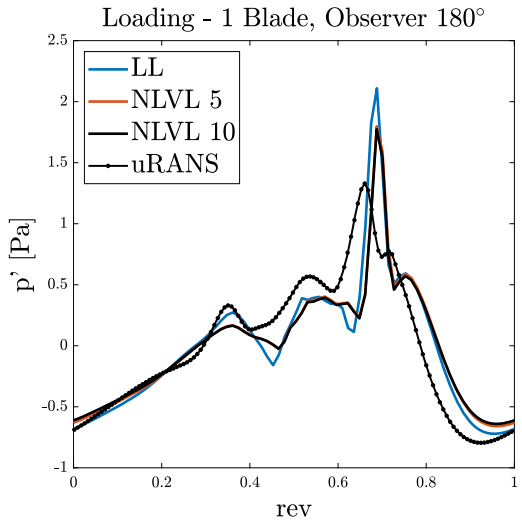

Fig. 15. Pressure fluctuation contribution due to loading noise over one revolution for a single blade of the rear propeller in the staggered configuration ($\frac{L_x}{R} = 5$ and $\frac{L_y}{R} = 1$) on xy plane. Convergence of the NLVL method is also shown. The set of observers ($r = 5R$) is defined in Fig. 4.

Data availability

Data will be made available on request.

References

[1] Polaczyk N, Trombino E, Wei P, Mitici M. A review of current technology and research in urban on-demand air mobility applications. In: Proceedings of the vertical flight society's 6th annual electric VTOL symposium; 2019.

[2] Silva C, Johnson W, Solis E, Patterson MD, Antcliff KR. VTOL urban air mobility concept vehicles for technology development. In: Proceedings of the 2018 aviation technology, integration, and operations conference; 2018.

[3] Zhou W, Ning Z, Li H, Hu H. An experimental investigation on rotor-to-rotor interactions of small UAV propellers. In: Proceedings of the 35th AIAA applied aerodynamics conference; 2017.

[4] Shukla D, Komerath N. Multirotor drone aerodynamic interaction investigation. Drones 2018;2(4):1–13. https://doi.org/10.3390/drones2040043.

[5] Schmitz FH, Yu YH. Theoretical modeling of high-speed helicopter impulsive noise. J Am Helicopter Soc 1979;24(1):10–9. https://doi.org/10.4050/JAHS.24.1.10.

[6] Yunus F, Grande E, Casalino D, Avallone F, Ragni D. Efficient low-fidelity aeroacoustic permanence calculation of propellers. Aerosp Sci Technol 2022;123:107438. https://doi.org/10.1016/j.ast.2022.107438.

[7] Casalino D, Barbarino M, Visingardi A. Simulation of helicopter community noise in a realistic urban environment. https://doi.org/10.2514/6.2010-4004, 2012.

[8] Yunus F, Casalino D, Avallone F, Ragni D. Efficient prediction of urban air mobility noise in a vertiport environment. Aerosp Sci Technol 2023;139:108410. https://doi.org/10.1016/j.ast.2023.108410.

[9] Bernardini G, Gennaretti M, Testa C. Spectral-boundary-integral compact-source formulation for aero-hydroacoustics of rotors. AIAA J 2016;54(11):3349–60. https://doi.org/10.2514/1.J054923.

[10] Ingraham D. Low-noise propeller design with the vortex lattice method and gradient-based optimization. In: AIAA SCITECH 2023 forum; 2023. p. 2039.

[11] Lopes LV. Compact assumption applied to monopole term of Farassat's formulations. J Aircr 2017;54(5):1649–63. https://doi.org/10.2514/1.C034048.

[12] Jo Y, Jardin T, Gojon R, Jacob MC, Moschetta J-M. Prediction of noise from low Reynolds number rotors with different number of blades using a non-linear vortex lattice method. In: 25th AIAA/CEAS aeroacoustics conference; 2019.

[13] Zanotti A, Algarotti D. Aerodynamic interaction between tandem overlapping propellers in eVTOL airplane mode flight condition. Aerosp Sci Technol 2022;124:107518. https://doi.org/10.1016/j.ast.2022.107518.

[14] Caccia F, Abergo L, Savino A, Morelli M, Zhou BY, Gori G, et al. Multi-fidelity numerical approach to aeroacoustics of tandem propellers in eVTOL airplane mode. https://doi.org/10.2514/6.2023-3221, 2023.

[15] Di Francescantonio P. A new boundary integral formulation for the prediction of sound radiation. J Sound Vib 1997;202(4):491–509. https://doi.org/10.1006/jsvi.1996.0843.

[16] Galimberti L, Morelli M, Guardone A, Zhou BY. Propeller noise prediction capabilities within SU2. In: Proceedings of the AIAA SCITECH 2023 forum; 2023. p. 1548.

[17] Yin J, De Gregorio F, Rossignol K-S, Rottmann L, Ceglia G, Reboul G, et al. Acoustic and aerodynamic evaluation of dlr small-scale rotor configurations within garteur ag26. CEAS Aeronaut J November 2024. https://doi.org/10.1007/s13272-024-00790-2.

[18] Tugnoli M, Montagnani D, Syal M, Droandi G, Zanotti A. Mid-fidelity approach to aerodynamic simulations of unconventional VTOL aircraft configurations. Aerosp Sci Technol 2021;115:106804. https://doi.org/10.1016/j.ast.2021.106804.

[19] Winckelmans GS. Topics in vortex methods for the computation of three- and two-dimensional incompressible unsteady flows. Ph.D. dissertation. California Institute of Technology; 1989.

[20] Cottet GH, Koumoutsakos PD. Vortex methods: theory and practice. Cambridge University Press; 2000.

[21] Cocco A, Colli A, Savino A, Masarati P, Zanotti A. A non-linear unsteady vortex lattice method for aeroelastic rotor loads evaluation. In: 48th European rotorcraft forum; 2022. p. 1–8.

[22] Savino A, Cocco A, Zanotti A, Tugnoli M, Masarati P, Muscarello V. Coupling mid-fidelity aerodynamics and multibody dynamics for the aeroelastic analysis of rotary-wing vehicles. Energies 2021;14(21):6979. https://doi.org/10.3390/en14216979.

[23] Piszkin ST, Levinsky E. Nonlinear lifting line theory for predicting stalling instabilities on wings of moderate aspect ratio. Tech. Rep. San Diego, CA: General Dynamics Convair Div.; 1976. https://api.semanticscholar.org/CorpusID:107820302.

[24] Cocco A, Savino A, Colli A, Masarati P, Zanotti A. A non-linear unsteady vortex-lattice method for rotorcraft applications. Aeronaut J 2024;128(1328):2308–30. https://doi.org/10.1017/aer.2024.55.

[25] Goitia H, Llamas R. Nonlinear vortex lattice method for stall prediction. MATEC Web Conf 2019;304:02006. https://doi.org/10.1051/matecconf/201930402006.

[26] Gori G, Davoli T, Rausa A, Zanotti A, Auteri F, Guardone A. Bayesian calibration of a low order aerodynamic model for the design of unconventional tail empennages. In: AIAA AVIATION 2023 forum; 2023. p. 4422.

[27] Farassat F. Linear acoustic formulas for calculation of rotating blade noise. AIAA J 1981;19(9):1122–30. https://doi.org/10.2514/3.60051.

[28] Zanotti A, Velo A, Pepe C, Savino A, Grassi D, Riccobene L. Aerodynamic interaction between tandem propellers in evtol transition flight configurations. Aerosp Sci Technol 2024;147:109017. https://doi.org/10.1016/j.ast.2024.109017.

[29] Drela M. Xfoil: an analysis and design system for low Reynolds number airfoils. In: Mueller TJ, editor. Low Reynolds number aerodynamics. Berlin, Heidelberg: Springer Berlin Heidelberg; 1989. p. 1–12.

[30] Viterna LA, Janetzke DC. Theoretical and experimental power from large horizontal-axis wind turbines. Tech. Rep. Cleveland, OH (United States): NASA Lewis Research Center; 1982.

[31] Thurman C, Boyd Jr DD, Buning P, Reboul G, Benoit C. NASA/ONERA collaboration on small hovering rotor broadband noise prediction using lattice-Boltzmann method and structured Navier-Stokes solvers. https://doi.org/10.2514/6.2024-3106.

[32] Economon TD, Palacios F, Copeland SR, Lukaczyk TW, Alonso JJ. SU2 an open-source suite for multiphysics simulation and design. AIAA J 2016;54(3):828–46. https://doi.org/10.2514/1.J053813.

[33] Economon TD, Palacios F, Alonso JJ. A viscous continuous adjoint approach for the design of rotating engineering applications. AIAA J 2013. https://doi.org/10.2514/6.2013-2580.

[34] Farrell PE, Piggott MD, Pain CC, Gorman GJ, Wilson CR. Conservative interpolation between unstructured meshes via supermesh construction. Comput Methods Appl Mech Eng 2009;198(33–36):2632–42. https://doi.org/10.1016/j.cma.2009.03.004.

[35] Rinaldi E, Colonna P, Pecnik R. Flux-conserving treatment of non-conformal interfaces for finite-volume discretization of conservation laws. Comput Fluids 2015;120:126–39. https://doi.org/10.1016/j.compfluid.2015.07.017.

[36] Jameson A, Schmidt W, Turkel E. Numerical solution of the Euler equations by finite volume methods using Runge Kutta time stepping schemes. In: 14th fluid and plasma dynamics conference; 1981. p. 1259.

[37] Spalart P, Allmaras S. A one-equation turbulence model for aerodynamic flows. In: Proceedings of the 30th aerospace sciences meeting and exhibit; 1994.

[38] Cakmakcioglu SC, Bas O, Mura R, Kaynak U. A revised one-equation transitional model for external aerodynamics. In: Proceedings of the AIAA AVIATION 2020 FORUM, virtual event; 2020.